Attenuation tomography of the western United States from ambient seismic noise

Jesse F. Lawrence[1] and Germán A. Prieto[2]

Received 12 July 2010; revised 11 March 2011; accepted 15 March 2011; published 15 June 2011.

[1] We show that the spatial coherency of the ambient seismic field can be used for attenuation tomography in the western United States. We evaluate the real portion of the spatial coherency with an elastic geometric spreading term (a Bessel function) and a distance dependent decay (an attenuation coefficient). In order to invert the spatial coherency, a weight stack inversion technique is applied. We recover phase velocity and attenuation coefficient maps at periods of 8–32s, which correspond to the elastic and anelastic structure at crustal and upper mantle depths. The phase velocity maps obtained by this method are of similar resolution to more standard two-station methods. The attenuation results provide an important complement to the information extracted from earthquake-based tomography. Several geological features are easily identifiable in the attenuation coefficient maps, such as the highly attenuating sedimentary basins along the West Coast of the United States, and the highly attenuating Yellowstone region, and the boundaries of the Snake River Plains.

Citation: Lawrence, J. F., and G. A. Prieto (2011), Attenuation tomography of the western United States from ambient seismic noise, *J. Geophys. Res.*, *116*, B06302, doi:10.1029/2010JB007836.

1. Introduction

[2] Traditionally, surface wave records from regional or teleseismic earthquakes are used at both global and regional scales to study the seismic velocity and attenuation structure of the Earth [e.g., *Mitchell*, 1995; *Romanowicz*, 2002; *Yang et al.* 2007; *Yang and Forsyth*, 2008]. The uneven and limited locations of earthquakes at plate boundaries, and the loss of high-frequency information due to intrinsic and scattering attenuation, limits resolution, especially for attenuation, in these studies.

[3] Imaging seismic attenuation of the crust and upper mantle is important for several reasons. First, seismic attenuation can be critical for discriminating between temperature and volatile content variations within the Earth when compared to seismic velocity [*Karato*, 1993; *Karato*, 2003; *Priestley and McKenzie*, 2006]. Knowledge of both velocity and attenuation structure are also important for correctly predicting ground motion from future large earthquakes [*Komatitsch et al.*, 2004; *Power et al.*, 2008]. Second, the seismic velocities found in sedimentary basins amplify seismic waves, but attenuation also reduces these amplitudes, and failing to account for attenuation may lead to higher ground motion amplitude predictions [e.g., *Olsen et al.*, 2006]. Third, by stripping the crustal and upper mantle attenuation from body wave attenuation measurements, it may be possible for future studies to better examine the attenuation structure deeper within the Earth.

[4] With increases in data quantity, computer power, and disk storage, seismologists have recently turned to the ambient seismic field (ASF) to study Earth's velocity structure [*Shapiro et al.*, 2005; *Sabra et al.*, 2005a, 2005b; *Yao et al.*, 2006; *Zheng et al.*, 2008]. By temporally averaging (to simulate azimuthal averaging of many sources) correlated records from two stations, it is possible to generate a stable empirical Green's function (EGF) for those two stations [*Weaver and Lobkis*, 2004; *Sabra et al.*, 2005b; *Sanchez-Sesma and Campillo*, 2006]. Dispersion curves of phase and group velocities obtained from these EGFs have been used to generate a plethora of high-resolution models of the crust and upper mantle [e.g., *Shapiro et al.*, 2005; *Yao et al.*, 2006; *Lin et al.*, 2008].

[5] While most prior studies focused on the phase of the EGFs, fewer studies have examined the amplitude information contained within EGFs [*Weaver and Lobkis*, 2001; *Larose et al.*, 2007; *Snieder and Safak*, 2006; *Kohler et al.*, 2007; *Prieto and Beroza*, 2008]. Similarly, greater attention has been paid to time domain correlation as compared to the frequency domain coherency [e.g., *Ekström et al.*, 2009; *Tsai and Moschetti*, 2010]. In the frequency domain the elastic portion of the Rayleigh wave within the EGF can be modeled as a zero-order Bessel function, J_0 (and/or the Hilbert transform Neumann function, Y_0) [*Morse and Ingard*, 1968; *Sanchez-Sesma and Campillo*, 2006; *Prieto et al.*, 2009; *Ekström et al.*, 2009; *Tsai and Moschetti*, 2010]. *Prieto et al.* [2009] demonstrated that the amplitudes of the frequency domain EGFs calculated for southern California can be explained with a geometric spreading term defined by the Bessel function

[1]Department of Geophysics, Stanford University, Stanford, California, USA.
[2]Departamento de Física, Universidad de los Andes, Bogotá, Colombia.

0148-0227/11/2010JB007836

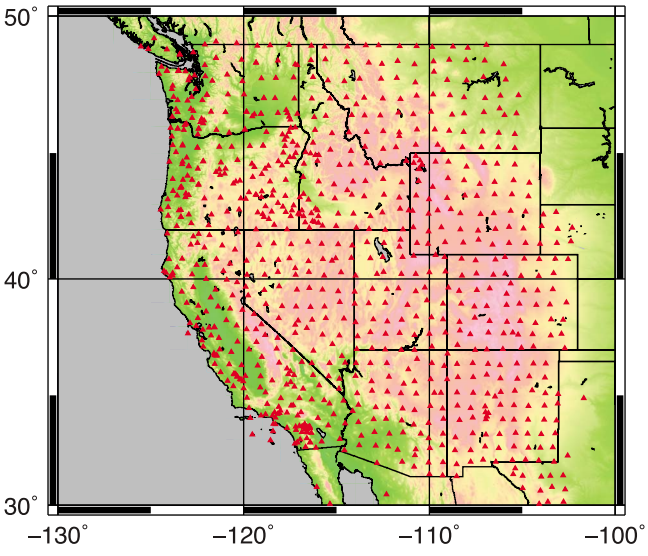

Figure 1. This map illustrates the locations of the seismic stations (red triangles) overlain on the topography of the western United States. The dense spacing of seismic stations provides an ideal gridded data set for tomographic inversion in this study region.

and a seismic attenuation term defined as an amplitude decay with distance.

[6] Here, we extend the one-dimensional attenuation method of *Prieto et al.* [2009] to image the lateral variation in seismic attenuation for the crust and upper mantle beneath the western United States (Figure 1). We first provide a general background describing the spatial autocorrelation method (SPAC) and its application to measuring seismic attenuation. We then describe the data and how it may be used to image lateral variations in frequency dependent phase velocity and attenuation coefficients. Finally, we present and discuss the observed attenuation structures within the western United States.

2. Background

[7] Here we provide a cursory overview of the SPAC method as it is applied to attenuation measurement. This study builds upon a larger volume of work that may be useful for understanding the methods and applications described here. For a more detailed introduction to SPAC, please see *Aki* [1957] and *Claerbout* [1968]. For a general background on EGFs we refer the reader to *Weaver and Lobkis* [2001]. Seismic tomography using EGFs is demonstrated by *Shapiro et al.* [2005]. The direct relationship between SPAC and the EGF is explicitly shown by *Yokoi and Margaryan* [2008] and *Tsai and Moschetti* [2010]. *Prieto and Beroza* [2008] demonstrates how amplitude is recovered (not just phase).

[8] In the time domain the correlation of whitened ambient seismic noise at two stations (A and B) yields a waveform resembling the empirical Green's function between the two. In the frequency domain, the prewhitened normalized correlation function is equivalent to the interstation coherency (more details on coherence calculation below). The real portion of the interstation coherency $\gamma_{AB}(\omega)$ can be represented by a zero-order Bessel function, J_0,

$$\mathrm{Re}[\gamma_{AB}(\omega)] = J_0(\omega r / C(\omega)), \tag{1}$$

where ω is the angular frequency, r is interstation distance, and C is phase velocity [*Aki*, 1957; *Morse and Ingard*, 1968; *Sanchez-Sesma and Campillo*, 2006; *Yokoi and Margaryan*, 2008; *Ekström et al.*, 2009]. *Ekström et al.* [2009] demonstrate that equivalent tomographic images result from frequency and time domain methods.

[9] However, because of attenuation, the observed interstation coherencies typically have lower amplitudes than the elastic model (the Bessel function) for any given station separation. The amplitude decay with distance can be described with a frequency-dependent exponential decay factor, $e^{-\alpha(f)r}$, where α is the frequency-dependent attenuation coefficient and r is the station separation [e.g., *Mitchell*, 1981, 1995]. This was used by *Prieto et al.* [2009] to measure both the phase velocity and attenuation coefficient and to estimate 1-D depth-dependent quality factor (Q) models for southern California. *Prieto et al.* [2009] stacked the real portion of the calculated coherency according to station separation for all station pairs in a network (e.g., Figure 2a). Then they performed a grid search for phase velocity at each frequency to reduce the misfit between the stacked real coherency and the Bessel function with distance (e.g., Figure 2b). Finally, a grid search was performed for attenuation coefficient at each frequency to reduce the elastic amplitudes to fit the stacked real coherency (e.g., Figure 2c). As a result, *Prieto et al.* [2009] generated frequency-dependent attenuation coefficient measurements that were inverted for depth-dependent Q. The frequency domain interstation coherency analysis (Figure 2a) is similar to the Fourier transform of the prewhitened time domain normalized cross-correlation analysis (Figure 2d) evaluated for all station separations.

[10] There are several factors that may contaminate the attenuation measurements obtained with the method of *Prieto et al.* [2009]. First, focusing and defocusing of Rayleigh waves as they pass through 3-D heterogeneous structures can change amplitudes [e.g., *Dalton and Ekström*, 2006a]. The array stacking method should minimize this effect by both averaging focusing and defocusing for a variety of azimuths across a broader area, although this has not been demonstrated. In this study, we attempt to reduce the effects of focusing during measurement but do not directly correct for focusing contaminations. Second, the ambient noise source may contaminate the ambient noise measurement of phase velocity and attenuation. *Harmon et al.* [2010] suggest that a nonuniform ambient seismic source field may contaminate phase velocity and attenuation coefficients by 1% and 100%, respectively, for a single plane wave noise source when measured with the method of *Prieto et al.* [2009]. Given that the resolved attenuation measurements of *Prieto et al.* [2009] vary by less than 10% for 1-month and 3-month stacks, in the presence of a time-varying source field [*Harmon et al.*, 2010], this effect for a yearlong coherency stack is considered minimal. Furthermore, the *Prieto et al.* [2009] results merge smoothly with those of *Yang and Forsyth* [2008] who studied longer-period surface waves from earthquakes. This

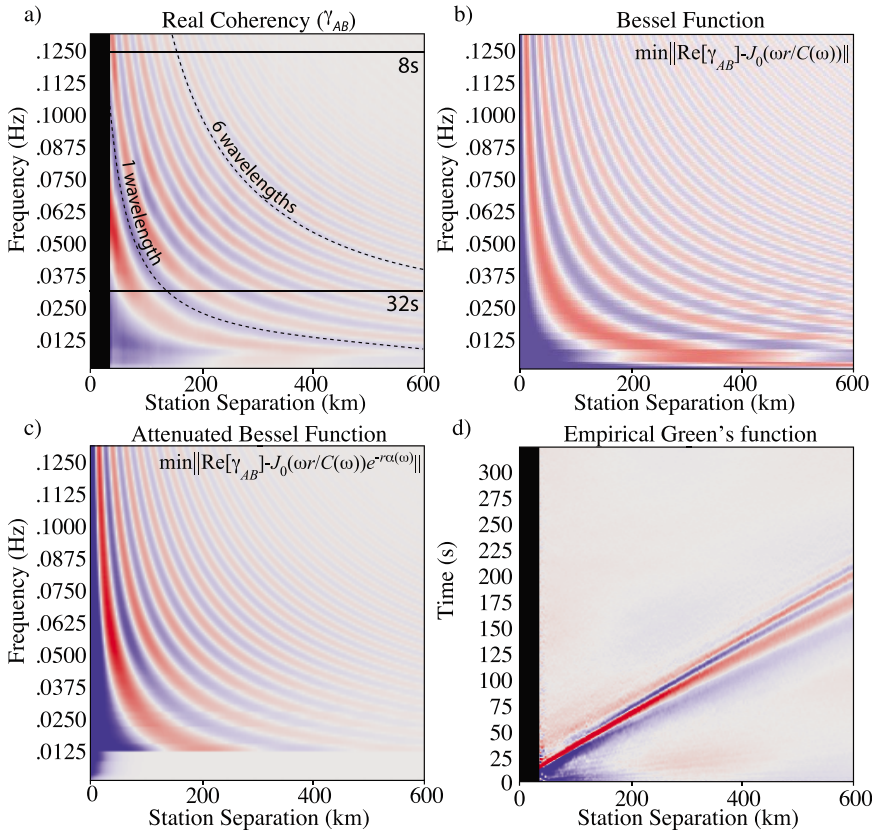

Figure 2. (a) A stack of all high signal-to-noise (SNR > 3) real interstation coherencies for USArray in 2007 and 2008. (b) The Bessel functions that best fits the stacked coherency in Figure 2a. (c) The attenuated Bessel function that best fits the stacked coherency in Figure 2a. (d) The inverse Fourier transform of the stacked coherency (cross-correlation). Figures 2b and 2c were minimized between 1 and 6 wavelengths (dashed lines in Figure 2a). This study focuses on results between 8 and 32 s (solid lines in Figure 2a). We do not use short station separations ($r < 30$; black rectangle) because the time interval (1 s) is less than 10% of the nominal Rayleigh wave travel time between stations ($t = r/C(\omega)$, where $r <$ 30 km, and $C(\omega) \approx 3$ km/s phase velocity).

suggests that the ambient seismic field measurements are at least consistent with earthquake measurements between 20 and 32 s.

[11] By dividing the data set into paths that cross major sedimentary basins and paths that do not, *Prieto et al.* [2009] demonstrated that the method could determine higher attenuation within the basins. Since the approach requires measurements of interstation coherency as a function of station spacing (e.g., Figure 2), many station pairs must be included. This requirement presents a challenge for resolving small-scale lateral variations in attenuation. Here, we extend the method of *Prieto et al.* [2009] to allow for lateral variations, and we apply our approach to USArray data recorded in 2007 and 2008.

3. Data

[12] All available broadband vertical-component data sampled at 1 Hz recorded at stations within the continuous western United States between 2007 and 2008 were downloaded, demeaned, detrended, and instrument corrected through SOD [*Owens et al.*, 2004]. Figure 1 illustrates the stations with sufficient data to be used in this study. The time-averaged interstation coherency is calculated for each station pair using all available common 2-h durations. The normalized interstation coherency, γ, is calculated for each station pair, AB, and each frequency, ω, as

$$\gamma_{AB}(\omega) = \left\langle \frac{u_A(\omega)u_B^*(\omega)}{\{u_A(\omega)\}\{u_B(\omega)\}} \right\rangle, \tag{2}$$

where $u(\omega)$ is the Fourier transform of the ground motion record, the asterisk indicates the complex conjugate, the curly brackets indicate the 20-point smoothed spectral density function, and the angle brackets indicate the time-averaged ensemble.

[13] Only station pairs with greater than 6 months of common data were evaluated. Bootstrap resampling over all available 24-h stacks per station pair provided estimates of the standard error of the interstation real coherency at each frequency. A signal-to-noise ratio (SNR) of the real part of the interstation coherency was calculated as the ratio of the maximum real coherency range to the maximum standard error of the real coherency between 8 and 32 s. Only station pairs with station separation greater than 30 km and less

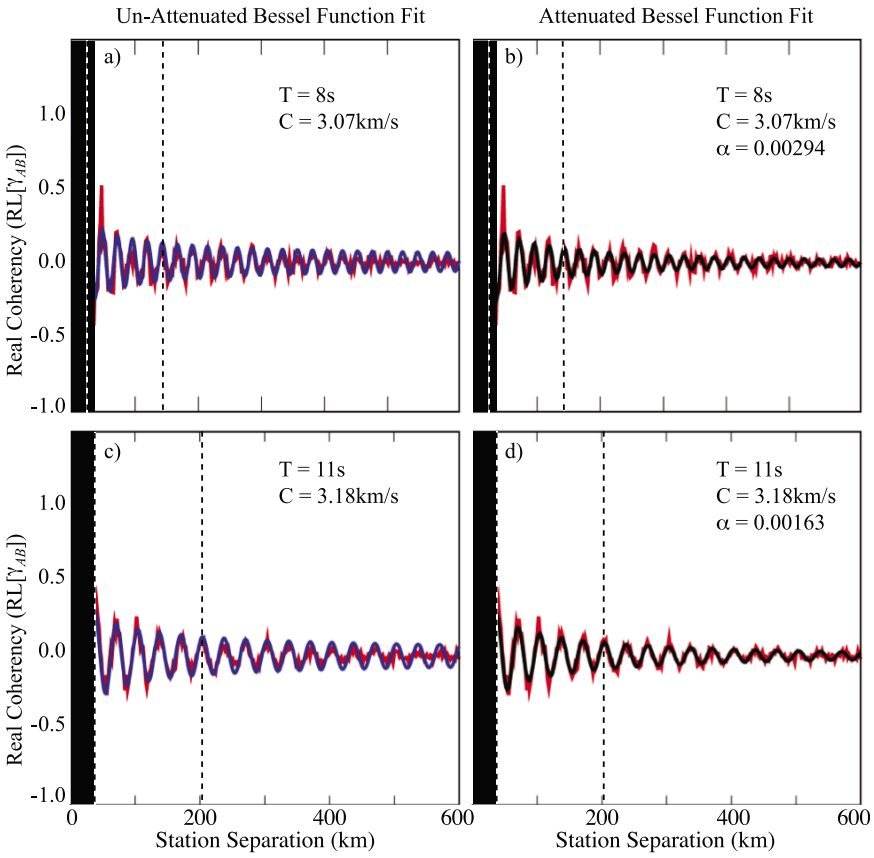

Figure 3. Stacked coherency estimates (red) for two frequencies (top = 8 s; bottom = 11 s) for the (left) unattenuated (blue) and (right) attenuated Bessel function (black) models. The misfits are minimized for station separations between 1 and 6 wavelengths (dashed lines), but the fit is improved at all separations between 30 and 600 km. The fit is not calculated for station separations shorter than 30 km (black rectangle).

than 600 km were used. At less than 30 km the sampling interval (1 s) is greater than 10% of the Rayleigh wave travel time between seismic stations. At greater than ~600 km, there are far fewer high SNR interstation coherencies.

[14] The data processing resulted in 76,587 high SNR (>3) interstation coherencies. A single stack of all high SNR coherencies for the data is illustrated in Figure 2. The application of the *Prieto et al.* [2009] technique to this data results in >99% and >95% fit (F) between the data for the attenuated and the unattenuated Bessel function models, respectively (Figure 2). Fit, F, is defined here as

$$F = 1 - \sum |\gamma_{obs} - \gamma_{the}| / \sum (|\gamma_{obs}| + |\gamma_{the}|)/2,$$

where the subscripts indicate observed and theoretical values of coherency and the summations are over all points. While the misfit is minimized for station separations between 1 and 6 wavelengths, the attenuated Bessel function model fits better than the unattenuated Bessel Function model for all station separations between 30 and 600 km, even for higher frequencies (shorter wavelengths) (Figure 3). The stack of western United States coherencies may be described with average phase velocity and attenuation coefficient curves illustrated in Figure 4. These average dispersions are used as the initial mean dispersions for the tomography described below.

4. Method

[15] The method of *Prieto et al.* [2009] must be adapted and extended to examine lateral variations in attenuation structure. First, we conceive of dividing a seismic array into many partially overlapping subarrays. We could then apply the *Prieto et al.* [2009] approach of stacking coherencies according to station separation and searching for the optimal phase velocity and attenuation coefficient using each subarray. Unfortunately, by stacking (averaging) data over broad overlapping subarrays, we would obtain aliased and damped measurements. Each measurement would represent a broad area, where variations within that area were averaged. Small-scale large amplitude anomalies might bias the results for the whole subarray. We can reduce the bias by upweighting interstation coherencies for station pairs that have greater sensitivity to the center of the subarray and downweighting station pairs with less sensitivity to the center of the array. However, the data would still be aliased and damped. Here we develop an inversion method to unalias these measurements and recover images that represent the "true" attenuation structure.

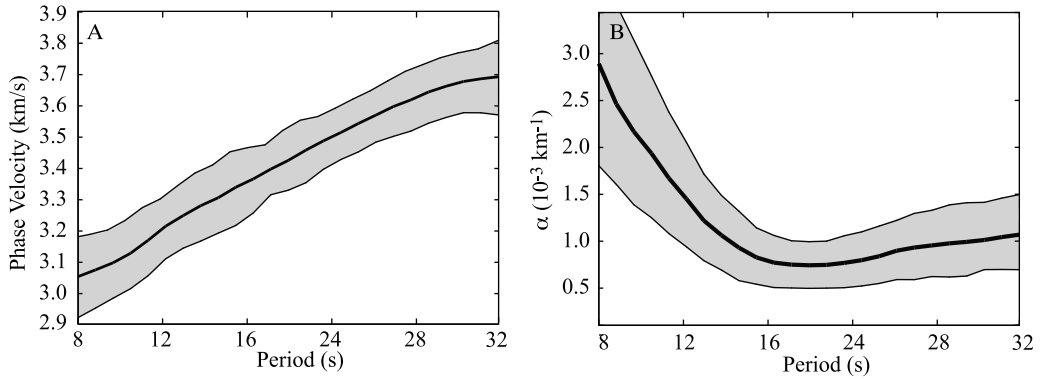

Figure 4. Average (bold line) (a) phase velocities and (b) attenuation coefficients by period calculated from an unweighted stack of all high signal-to-noise USArray data recorded in 2007 and 2008. The gray regions illustrate the 1-sigma standard deviation measurements from the mean at each period.

[16] In order to obtain unaliased maps of the phase velocity and attenuation coefficients for the western United States, the following procedure is used. For each period, the research area (the western United States) is parameterized by an array of 6400 0.25° × 0.25° grid cells. We sample periods between 8 s and 32 s at 1 s intervals. Values of phase velocity, C, and attenuation coefficient, α, are estimated for each grid cell (when possible) from the coherency measurements at the stations located near the grid cell.

[17] For any particular grid cell, the real part of the coherency is stacked into bins according to interstation separation at 2 km bin intervals. We regionalize the data for tomographic inversion by upweighting coherencies with paths closer to the grid cell of interest and downweighting paths farther from the grid cell. Weighting is described in more detail below. We require that (1) more than 500 coherencies be incorporated in each stack and (2) at least 20 distinct interstation distances are occupied by data.

[18] From the subarray coherency stacks, a three-iteration stepwise grid search identifies the optimal phase velocity and attenuation coefficient for each period and each grid cell by minimizing the L1 misfit between the real subarray coherency stack and a damped Bessel function,

$$\min \parallel \mathrm{Re}[\gamma_{AB}(\omega)] - J_0(\omega r / C(\omega)) e^{-\alpha(\omega) r} \parallel . \qquad (3)$$

For each iteration, we first search for phase velocity and then attenuation coefficient. The L2 misfit provides similar results as L1; however, L1 deemphasizes outliers caused by noisy interstation coherencies. The algorithm efficiently searches the phase velocity range 2.5–5 km/s and the attenuation coefficient range 10^{-5}–10^{-1} with precision to 10^{-3} km/s and 10^{-6}, respectively. We find that the results were less stable at station separations less than one wavelength, so only data for station pairs greater than one wavelength were used. At periods greater than ~6 s, 95% confidence intervals (from chi-square tests of the grid search) for stacks with more than 500 station pairs are generally better 1% for phase velocity and 3% for attenuation coefficients, respectively. Interstation distances are limited to fewer than six wavelengths because geometric spreading and seismic attenuation often reduce the coherent ASF below the incoherent noise at between six and eight wavelengths.

[19] The weight-averaged real subarray coherency depends on (1) the weighting (w) and (2) the data (d). While many weighting schemes could be chosen, it is important to select an appropriate weighting scheme that (1) regionalizes the data, (2) provides sufficient data for stable stacks, and (3) supports stable tomographic inversion. The weighting must upweight interstation coherencies (and the inversion sensitivity kernel) in a localized region and downweight or null-weight interstation coherencies (and sensitivity kernels) farther from the desired region. After some trial and error we converged on a weight (w) for each interstation coherency of the form

$$w_{ijk} = \sum_{o=1}^{NX_{path_i}} \sum_{p=1}^{NY_{path_i}} \sum_{l=j-1}^{j+1} \sum_{m=k-1}^{k+1} \frac{\delta_{ol}\delta_{pm}}{(1 + |l-j| + |m-k|)}, \qquad (4)$$

where NX_{pathi} and NY_{pathi} are the lateral dimensions of the 2-D grid cell array, o and p designate the lateral positions of the grid cells along the ith interstation raypath, j and k indicate position of the central grid cell for each stack, and l and m are the lateral offsets from the central grid cell position. Figure 5 illustrates the application of this weighting scheme for several central stack grid cell locations and interstation paths. The weight stack, D_{jk}, of the data, d_i, (attenuation or phase velocity) for the ith station pair and the grid cell at coordinates (j, k) is $D_{jk} = \sum_{i=1}^{N_{data}} d_i\, w_{ijk} / \sum_{i=1}^{N_{data}} w_{ijk}$, where N_{data} is the number of high signal-to-noise ratio interstation coherencies.

[20] Greater than 5320 stacked attenuation and phase velocity measurements were obtained for each period. However, the stacking processes necessary for SPAC damps [*Tsai and Moschetti*, 2010] and aliases measurements for stacked data because the data sensitivities extend outside the grid cell of interest. Therefore we must perform a tomographic inversion to recover the "true" structure from the aliased data. This is achieved by also stacking the sensitivity kernels in the same manner as the data. The weight stacked kernel K_{ijk} for the ith station pair and the (jth, kth) grid cell is given by $K_{ijk} = k_{ijk}\, w_{ijk} / \sum_{i=1}^{N_{data}} k_{ljk}\, w_{ljk}$ (in practice each jk pair is vectorized). Note that the summed kernels over all station pairs and all grid cells is 1 ($\sum_{i=1}^{N_{data}} \sum_{j,k=1}^{N_{Node}} K_{ijk} = 1$).

[21] The appropriate kernel, k_{ijk}, to use for phase velocity and attenuation coefficients calculated from a zero-order

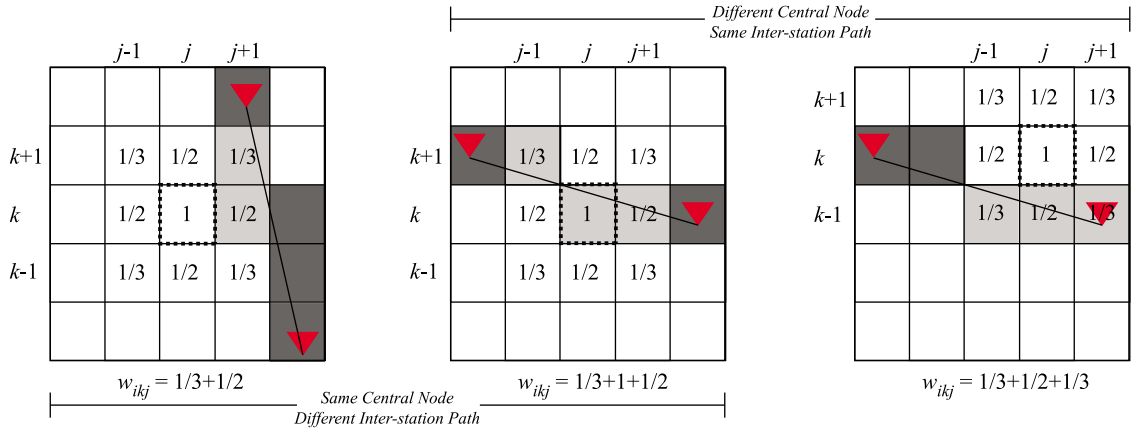

Figure 5. Three weights (w_{ijk}) graphically calculated for different ith station pairs and for different central stack positions (j, k) within the array. The left and center weights have a common stack center (dashed outline) and different raypaths (black line) between stations (red triangles). The right and center weights are for different stack centers, for the same station pair. The numbers indicate the relative weighting for any path intersecting with that grid cell. The gray boxes indicate grid cells where the raypath intersects. The light gray boxes indicate grid cells where the path and weight overlap.

Bessel function has not been theoretically evaluated. The measurements are extremely frequency-limited, resulting in finite frequency sensitivity kernels that ring in the spatial domain. For simplicity in form and calculation, we estimate the sensitivity kernel as the infinite-frequency station-station raypath divided among 0.25° × 0.25° by 1 s grid cells. The infinite-frequency raypath approximation is computationally faster that the finite-frequency approximation, which allowed us to experiment with different weighting schemes. Mathematically, the kernel for each grid cell is $k_{ijk} = r_{ijk}/\sum_{n,m=1}^{N_{node}} r_{lmn}$, where r_{ijk} is the interstation range for the ith station pair divided into each (j, k) grid cell.

[22] In matrix notation, the sensitivity kernel matrix **K**, data **D**, and model **m** can be solved linearly using LSQR [*Paige and Saunders*, 1982]. The forward model takes the form

$$\begin{bmatrix} \mathbf{K} \\ \varepsilon\mathbf{L} \end{bmatrix} \mathbf{m} = \begin{bmatrix} \mathbf{D} \\ \mathbf{0} \end{bmatrix}, \tag{5}$$

where **L** is the first derivative roughness matrix, ε is the roughness weighting scalar, and **0** is a vector of zero value data points. We invert both phase velocity and attenuation coefficients using the absolute values rather than the perturbation from the mean because the attenuation perturbations are extremely high for periods where the mean attenuation coefficient is low (Figure 4). Given a linear damping, **L**, the high attenuation anomalies in the middle-to-long period range (>12 s) become unstable using the perturbation parameterization. To ensure nonnegative attenuation values for near-zero model coefficients, we apply a nonnegative constraint in the QR operator.

[23] To improve inversion stability at each period we smooth in both the spatial and period dimensions. For the phase velocity and attenuation coefficient maps calculated at each period, T_i, we invert only the data corresponding to T_i and $T_{i\pm1}$. Consequently, similarities observed between inverted maps calculated at more disparate periods (e.g., $T_{i\pm3}$) must result from the data and grid cell geometry, not the smoothing constraint. Smoothing across period is justified because, within the 8–32 s period range, Rayleigh wave phase velocities and attenuation coefficient change gradually with period even for the extremely low-velocities and high attenuations observed in shallow sedimentary basins [e.g., *Shapiro et al.*, 2005; *Prieto et al.*, 2009].

[24] Appropriate damping, ε, was attained by examining the difference in model outcomes for inversions having 10 different bootstrapped data sets and three 1/3 grid cell offsets in the latitude and longitude directions. An appropriate ε was assumed where the second derivative of the standard error of the model is maximized, similar to *Boschi et al.* [2006]. In other words, the damping is optimum when the marginal return of reducing or increasing the regularization constraint is maximized. Figure 6 graphically demonstrates the choice of ε for the 12 s attenuation coefficient inversion and illustrates the uncertainty for damping chosen for each period of the inversions.

5. Results

[25] The most optimal 8–32 s phase velocity maps calculated here (Figure 7) are comparable to, with marginally lower resolution, the phase velocity maps obtained using two-station frequency-time analysis [e.g., *Lin et al.*, 2008], eikonal tomography method [e.g., *Lin et al.*, 2008], or two-station Bessel function analysis [*Ekström et al.*, 2009]. A comparison of these maps with those of *Lin et al.* [2008] is provided in the Auxiliary Material (Figure S1).[1] As with prior studies, low seismic velocities are observed at short periods for the large sedimentary basins such as the Central Valley in California, and high velocities are observed for the Sierra Nevada and Cascadia ranges. As discussed above, the subarray stacking technique limits the model resolution for seismic velocity but is necessary to make stable attenuation measurements. Despite this averaging, an appropriate

[1] Auxiliary materials are available in the HTML. doi:10.1029/2010JB007836.

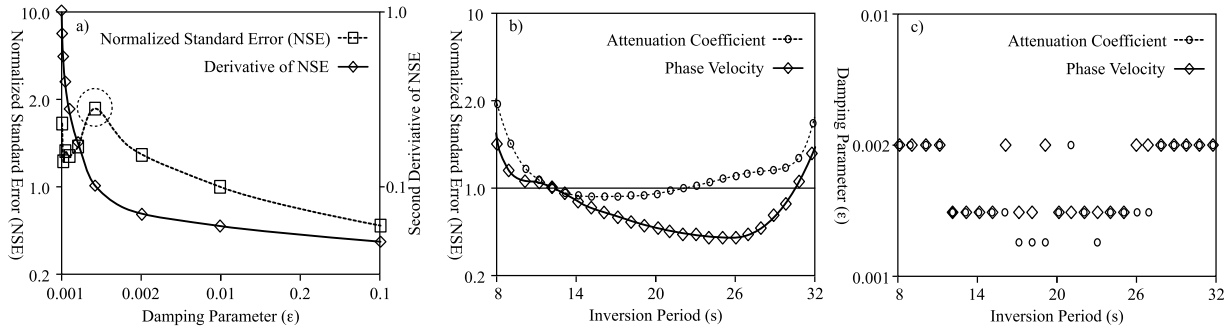

Figure 6. (a) The (diamonds) normalized 12 s attenuation coefficient model standard error and the (squares) second derivative of standard error with respect to the damping parameter. The standard errors are normalized by the standard error at the optimal damping parameter at $\varepsilon = 0.00125$. The standard error of the model is calculated for ten bootstrapped data sets with nine 1/3 grid cell shifted inversions. The (b) standard error (normalized to the 12-s optimal standard error in Figure 6a for the (c) optimal damping parameter, ε, for each period for which the inversions were calculated (normalized to the standard error at 12 s). The damping parameters for the phase velocity inversions were normalized by the ratio of the mean velocity to the mean attenuation coefficient at each period. The phase velocity standard errors were normalized to the 12 s standard error. The increasing error near 8 and 32 s suggests the limits of the resolvable frequencies for this method.

weighting provides comparable velocity structure results to the two-station methods. Hereafter we focus on the attenuation model, which is the main result of this study.

[26] The weight-stack inversion technique generates high-resolution attenuation maps that show interesting geological features. The attenuation maps between 8 and 32 s illustrate very high attenuation for the Pacific Northwest [e.g., *Hwang and Mitchell*, 1987] and Yellowstone [e.g., *Clawson et al.* [1989] and high attenuation along the west coast [e.g., *Phillips and Stead*, 2008]. The 8-s seismic attenuation coefficient maps also exhibit particularly strong attenuation in California's Central Valley. In the 24 s attenuation map, the Snake River Plain is more attenuating (albeit moderately so) relative to the surrounding terrains.

[27] The 8-, 12-, and 24-s attenuation coefficient maps are inverted independently, so similarities between models represent the data, not inverse regularization. The attenuation maps reduce the data misfit by 78%, 64%, and 68% relative to a laterally constant attenuation coefficient for the 8, 12, and 24 s inversions, respectively. To test the robustness of the method, we perform a bootstrap resampling, with nearly identical results (<2% model variance) for the majority of the attenuation model space. We masked the northeast quadrant of the maps due to moderate (2–10%) model variance between the bootstrapped model and mean inverted attenuation model.

[28] To further test the resolution of the inversion process, we performed checkerboard tests in the presence of noise (Figure 8). We multiply the sensitivities (K) and a checkerboard patterned model (**m**) to obtain a theoretical data (**D**) corresponding to that checkerboard pattern. We add a stochastic Gaussian variance to the theoretical data proportional to the variance between the observed data and the estimated data from the best fit inversion model. We then invert the theoretical data using equation (4), for a new model to determine how well the inversion recovers the checkerboard pattern. For one example checkerboard test, we gradually alternate between the checkerboard pattern in the *i*th period (Figures 8g–8i) and a 20% lower amplitude checkerboard pattern for the $i \pm 1$ periods (Figures 8a–8c and 8j–8l). In a second case, we alternate between the normal and reversed checkerboard pattern between each period. The first grants higher lateral resolution due to smoothing constraints between adjacent periods. This is more representative of phase velocity and attenuation data and inverted models, which vary gradually with frequency. The second case describes an instance where the phase velocity and attenuation coefficient change very rapidly with frequency as a worst-case scenario. The checkerboard pattern is recovered well in both instances at a 200 km wavelength. Reduced amplitudes are observed in the northeast corner where less data present.

[29] Alternate weighting schemes were tested, with similar results. Weighting schemes with w_{ijk} proportional to a/r and a/r^2, $a/r^{1/2}$, e^{-ar}, where r is the distance from the central grid cell provided similar results and a is a constant. We limited r to less than a, such that the weighting reaches a maximum of 1 in our tests. Inversions where weighting is only applied within a cutoff radius, $r < r_c$, provide better fidelity of short-wavelength features; averaging over a smaller area acts to damp short-wavelength variations less. Measurements obtained with lesser weighting gradients, dw/dr, average over a larger areas, resulting in more damped measurements. A constant weight for all distances can result in identical results for adjacent measurements, leading to data aliasing. Measurements obtained with much larger (e.g., >3X) lateral weighting gradients than the $1/r$ scheme tend to become less stable because insufficient station pairs are upweighted. At a grid cell spacing of 0.25°, the nonzero weighting region of the chosen weighting scheme has a lateral dimension of 0.75°, which is equivalent to that of the average station spacing.

6. Discussion

[30] The results show that the amplitude information contained within ambient seismic records may be useful for attenuation tomography. The subarray ASF inversion method

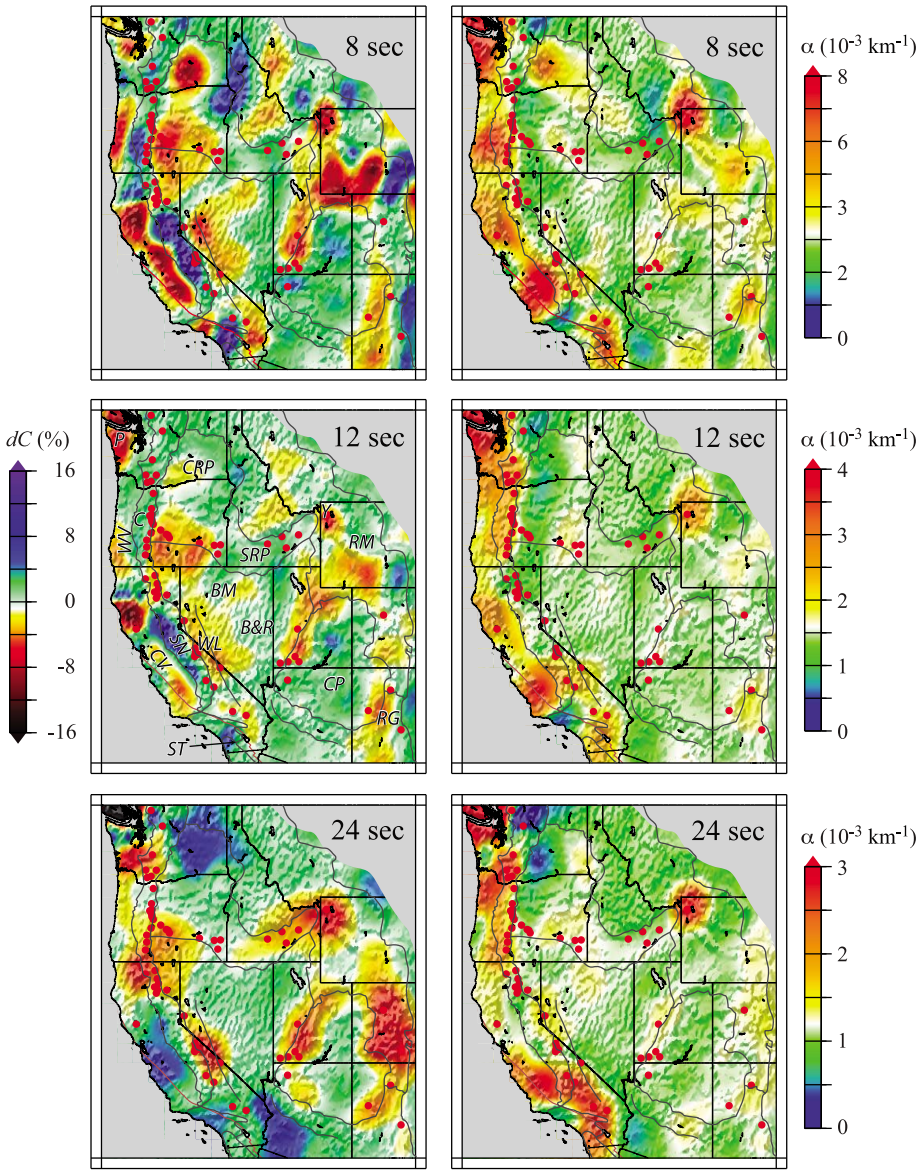

Figure 7. Maps of (left) phase velocity perturbation and (right) attenuation coefficients across the western United States inverted from (top) 8, (middle) 12, and (bottom) 24 s period ambient noise. Geologic terrain boundaries (thick black lines) and Holocene volcanoes (red circles) and state boundaries (thin black lines) are plotted for reference (http://earthquake.usgs.gov/earthquakes/). Regions referenced in the text are labeled: Battle Mountain (BM), Basin and Range (BR), Cascade Volcanic Arc (C) Columbia River Plateau (CRP), Colorado Plateau (CP), California Central Valley (CV), Puget Sound (P), Rio Grand Rift (RG), Rocky Mountains (RM), Salton Trough (ST), Sierra Nevada (SN), Snake-River Planes (SRP), Walker Lane (WL), Willamette Valley (WV), Yellowstone (Y). Poorly resolved regions are masked with gray.

presented here, while yielding marginally lower-resolution phase velocity images than two-station ASF methods, gives additional information (attenuation) that may be important for resolving nonuniqueness in geodynamical interpretation of velocity anomalies and, at the shorter period end of the spectrum, for seismic hazard analysis.

[31] Despite significant differences in data and methodology, the results presented here bear substantial similarity to the *Lg* attenuation maps of *Phillips and Stead* [2008]. Highly attenuating regions are observed in the Pacific Northwest, along the west coast, and near Yellowstone. Differences between *Phillips and Stead* [2008], *Lawrence et al.* [2006], and this study likely arise from the differing depth sensitivities (hundreds of kilometers to crustal depth range) and distinct data types (teleseismic body waves and *Lg* waves versus ambient noise) with differing frequency contents. Note that the maps presented here contain depth extent information in the frequency dispersion, whereas those of *Lawrence et al.* [2006] and *Phillips and Stead* [2008] do not. The depth sensitivity will provide an opportunity for future investigations to generate 3-D (two lateral and one depth dimension) *Q* models. Furthermore, correcting body

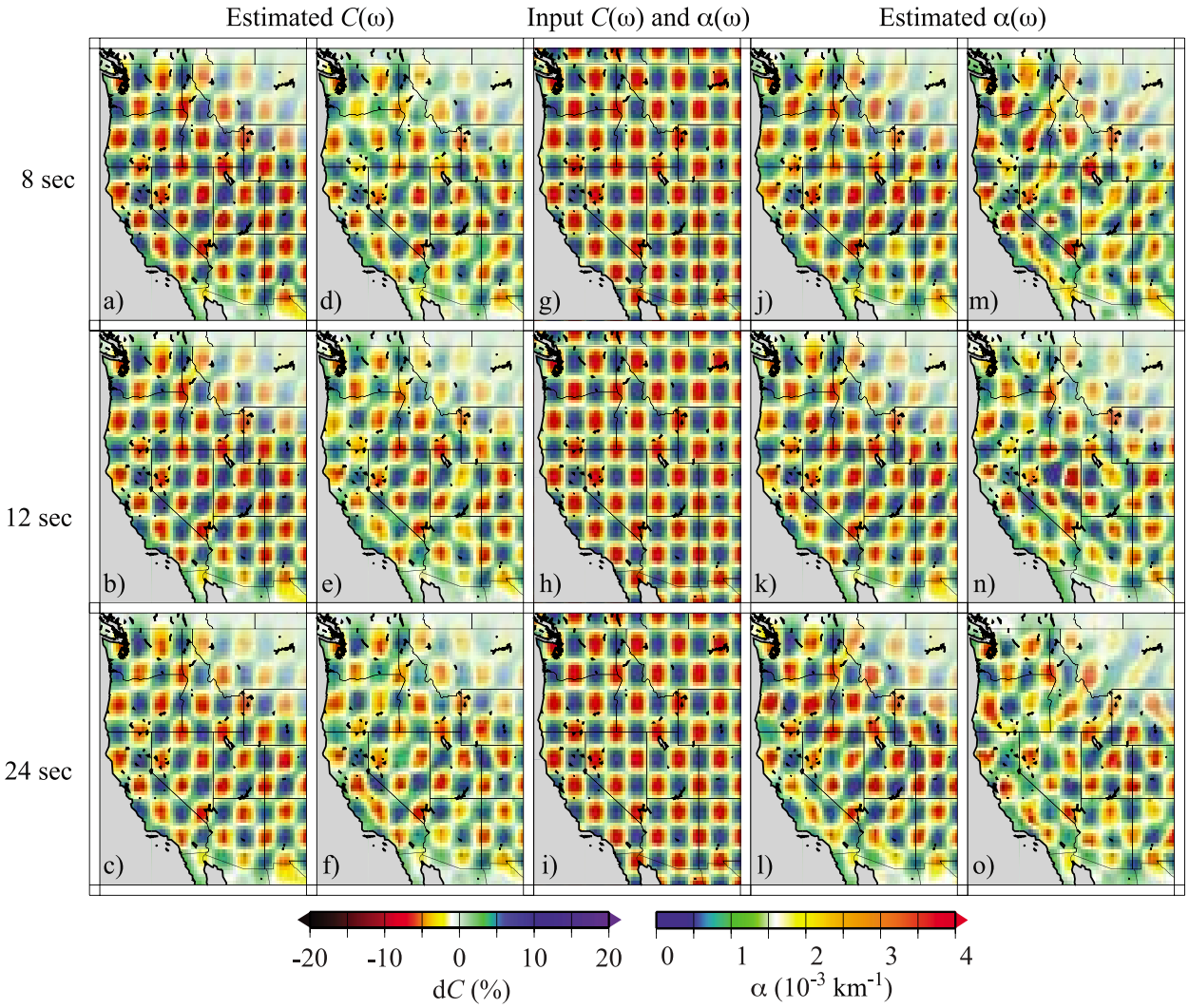

Figure 8. Checkerboard tests. Shown is the (a–c) phase velocity and (j–l) attenuation coefficient checkerboard model recovered from the inversion process at 8, 12, and 24 s periods and (g–i) the input model patterns for the *i*th period. In this case, the $i \pm 1$ s period input model pattern is 20% reduced. (d–f) Equivalent to Figures 8a–8c and (m–o) equivalent to Figures 8j–8l except where the pattern is reversed for the $i \pm 1$ s period input model. The checkerboard inversion is conducted with added stochastic variance that has a similar distribution to the variance between the observed data and the data estimated from the best fit model.

wave attenuation with shallow ambient noise attenuation may provide a mechanism to view deeper into the mantle using body wave attenuation tomography.

[32] The seismic attenuation presented here does not differentiate scattering from intrinsic attenuation. It is likely that the seismic attenuation we measure represents a combination of both scattering and intrinsic attenuation. The strongest high-attenuation anomalies correlate with low seismic velocity anomalies beneath large sedimentary basins such as the California Central Valley, Oregon Willamette Valley, and the Puget Sound Basin along the west coast [e.g., *Hwang and Mitchell*, 1987; *Pratt and Brocher*, 2006], particularly for the 8 s maps, which are more sensitive to shallower structure. This indicates that ground motion simulations [e.g., *Olsen et al.*, 2006] that lack lateral and 3-D seismic attenuation structure potentially overestimate the amplification due to the low seismic velocities in sedimentary basins. The northwestern portion of the Columbia River valley is highly attenuating at short periods, which is consistent with the hypothesis of *Pujol and Smithson* [1991] that scattering from shallow basalt layering, fractures, and vesicles may result in elevated scattering attenuation.

[33] The Yellowstone high-attenuation anomaly correlates well with a low seismic velocity anomaly, suggesting a common source. This high attenuation may result from high temperatures [*Xie*, 2002] and/or partial melt in the crust [*Fan and Lay*, 2003] related to the Yellowstone volcanism, high geothermal heat flow, and an abundance of hydrothermal activity including geysers [e.g., *Smith and Braile*, 1994]. Holocene volcanoes (http://earthquake.usgs.gov/earthquakes/) spatially correlate with greater than average attenuation and low seismic velocity at longer periods (>18 s). At shorter

periods, this correlation is overwhelmed by the signature of sedimentary basins. The long-period correlation of high attenuation and low seismic velocity with volcanism is consistent with high temperatures [e.g., *Karato*, 1993], suggesting that the long-period seismic attenuation and phase velocity maps illuminate the source region of volcanic melts. The distinct difference between Yellowstone and the Snake River Plain attenuation suggests that seismic velocity and attenuation may be particularly sensitive to regions with ongoing pervasive volcanism and less sensitive to areas where volcanism has subsided. The coherent pattern of marginally elevated attenuation and decreased seismic velocity of the Snake River Plain at long periods (>18 s) may indicate long-term thermal or chemical alteration of the crust/mantle.

[34] The elevated attenuation anomaly in north central Nevada at longer periods (>20 s) correlates with the Battle Mountain high heat flow region, which may be caused by hydrothermal and magmatic activity from 1 to 20 km depth [e.g., *Rodriguez and Williams*, 2001]. The Walker Lane, a broadly distributed zone of strike-slip and normal fault systems east of the Sierra Nevada Range, is highly attenuating at short and long periods. The Walker Lane high attenuation correlates with a low-viscosity compliant zone in the lower crust that accommodates the extensive observed strain [e.g., *Hammond et al.*, 2009]. Increased scattering due to extensive fractures/faults in the middle to shallow locked region of the crust [*Savage and Burford*, 1973] could cause strong scattering attenuation. The Walker Lane high-attenuation zone continues south to the Salton Trough, where strike-slip, normal faults intersect geothermal fields [*Lachenbruch and Sass*, 1978]. In contrast to deforming and magmatic regions, stable continental blocks such as the Colorado Plateau and Northern Rocky Mountains are low attenuating regions surrounded by more attenuating regions such as the Rio Grande Rift.

[35] Three-dimensional velocity structure may (de)focus seismic energy along velocity heterogeneities, leading to amplitude anomalies not corresponding to attenuation [*Dalton and Ekström*, 2006b; *Tian et al.*, 2009]. The effect of elastic heterogeneities must be taken into account prior to analyzing amplitude information [*Dalton and Ekström*, 2006a, 2006b]. The azimuthal averaging inherent in our weight-stacks should in theory reduce the effects of focusing. The maps in Figure 5 show both correlated and anticorrelated velocity and attenuation features, as is expected for a thermally, structurally, and chemically heterogeneous crust and mantle. If our measurements were strongly affected by focusing, we would expect only anticorrelated anomalies. Similarly, while source heterogeneity may contaminate the observed attenuation structure to some degree (as hypothesized by *Harmon et al.* [2010]), this effect must be minor compared to the actual attenuation variation observed in the western United States. If the heterogeneous source were responsible for the observed attenuation anomalies, the observed attenuation anomalies would correlate with network geometry, not with tectonic features.

7. Future Work

[36] It is unclear yet how applicable this new ASF stacking and inversion method will be for imaging attenuation structure with other seismic networks. This method requires many stations at many distances to ensure stable results. Applying this method to smaller and denser arrays will require scaling to shorter wavelengths and therefore higher frequencies, which are more applicable to shallower structure. Future focused studies of smaller-scale regions with a dense array may yield new insight into the mechanics related to attenuation scattering in basins and the hydrothermal influence on attenuation in volcanic systems. The extension of this analysis to 3-D Q (two lateral and one depth dimension rather than two lateral and one period dimension) will be challenging as scattering attenuation and intrinsic attenuation may not be separable.

8. Conclusions

[37] We have shown for the first time that attenuation tomography can be achieved with the ASF. At high frequencies the ASF attenuation coefficients should be helpful in modeling attenuation within major sedimentary basins. Future analyses may increase the resolution either regionally through increasingly dense seismic networks (such as Southern California or HiNet) or advances in the methodology. High-resolution attenuation tomography of regions like the L.A. Basin will provide important constraints for long-period ground motion prediction. At longer periods, the combination of elastic and anelastic information provides complimentary information about Earth's compositional and thermal structure.

[38] **Acknowledgments.** We thank Greg Beroza and Simon Klemperer for providing feedback and two reviewers for constructive comments and thorough reviews.

References

Aki, K. (1957), Space and time spectra of stationary stochastic waves, with special reference to microtremors, *Bull. Earthq. Res. Inst.*, *35*, 415–457.

Boschi, L., T.W. Becker, G. Soldati, and A. M. Dziewonski (2006), On the relevance of Born theory in global seismic tomography, *Geophys. Res. Lett.*, *33*, L06302, doi:10.1029/2005GL025063.

Claerbout, J. F. (1968), Synthesis of a layered medium from its acoustic transmission response, *Geophysics*, *33*(2), 264–269, doi:10.1190/1.1439927.

Clawson, S. R., R. B. Smith, and H. M. Benz (1989), P wave attenuation of the Yellowstone caldera from three-dimensional inversion of spectral decay using explosion source seismic data, *J. Geophys. Res.*, *94*(B6), 7205–7222, doi:10.1029/JB094iB06p07205.

Dalton, C. A., and G. Ekström (2006a), Global models of surface-wave attenuation, *J. Geophys. Res.*, *111*, B05317, doi:10.1029/2005JB003997.

Dalton, C. A., and G. Ekström (2006b), Constraints on global maps of phase velocity from surface-wave amplitudes, *Geophys. J. Int.*, *167*, 820–826, doi:10.1111/j.1365-246X.2006.03142.x.

Ekström, G., G. A. Abers, and S. C. Webb (2009), Determination of surface-wave phase velocities across USArray from noise and Aki's spectral formulation, *Geophys. Res. Lett.*, *36*, L18301, doi:10.1029/2009GL039131.

Fan, G.-W., and T. Lay (2003), Strong Lg attenuation in the Tibetan Plateau, *Bull. Seismol. Soc. Am.*, *93*(5), 2264–2272, doi:10.1785/0120030052.

Hammond, W. C., C. Kreemer, and G. Blewitt (2009), Geodetic constraints on contemporary deformation in the northern Walker Lane: 3. Central Nevada seismic belt postseismic relaxation, in *Late Cenozoic Structure and Evolution of the Great Basin–Sierra Nevada Transition*, edited by J. S. Oldow and P. H. Cashman, *Spec. Pap. Geol. Soc. Am.*, 447, 33–54.

Harmon, N., C. Rychert, and P. Gerstoft (2010), Distribution of noise sources for noise derived Green's functions, *Geophys. J. Int.*, *183*, 1470–1484, doi:10.1111/j.1365-246X.2010.04802.x.

Hwang, H. J., and B. J. Mitchell (1987), Shear velocities, Q and the frequency dependence of Q in stable and tectonically active regions from surface wave observations, *Geophys. J. R. Astron. Soc.*, *90*, 575–613.

Karato, S.-I. (1993), Importance of anelasticity in the interpretation of seismic tomography, *Geophys. Res. Lett.*, *20*, 1623–1626, doi:10.1029/93GL01767.

Karato, S.-I. (2003), Mapping water content in the upper mantle, in *Inside the Subduction Factory*, vol. 138, edited by E. J. M. Eiler, pp. 135–152, AGU, Washington, D. C.

Kohler, M. D., T. H. Heaton, and S. C. Bradford (2007), Propagating waves in the steel, moment-frame factor building recorded during earthquakes, *Bull. Seismol. Soc. Am.*, *97*(4), 1334–1345, doi:10.1785/0120060148.

Komatitsch, D., Q. Liu, J. Tromp, P. Suss, C. Stidham, and J. H. Shaw (2004), Simulations of ground motion in the Los Angeles Basin based upon the Spectral-Element Method, *Bull. Seismol. Soc. Am.*, *94*, 187–206, doi:10.1785/0120030077.

Lachenbruch, A. H., and J. H. Sass (1978), Models of an extending lithosphere and heat flow in the Basin and Range Province, in *Cenozoic Tectonics and Regional Geophysics of the Western Cordillera*, edited by R. B. Smith and G. P. Eaton, *Mem. Geol. Soc. Am.*, 152, 209–250.

Larose, E., P. Roux, and M. Campillo (2007), Reconstruction of Rayleigh-Lamb dispersion spectrum based on noise obtained from an air-jet forcing, *J. Acoust. Soc. Am.*, *122*(6), 3437–3444, doi:10.1121/1.2799913.

Lawrence, J. F., P. M. Shearer, and G. Masters (2006), Mapping attenuation beneath North America using waveform cross-correlation and cluster analysis, *Geophys. Res. Lett.*, *33*, L07315, doi:10.1029/2006GL025813.

Lin, F., M.P. Moschetti, and M.H. Ritzwoller (2008), Surface wave tomography of the western United States from ambient seismic noise: Rayleigh and Love wave phase velocity maps, *Geophys. J. Int.*, *173*, 281–298.

Mitchell, B. J. (1981), Regional variation and frequency dependence of Qβ in the crust of the United States, *Bull. Seismol. Soc. Am.*, *71*, 1531–1538.

Mitchell, B. J. (1995), Anelastic structure and evolution of the continental crust and upper mantle from seismic surface wave attenuation, *Rev. Geophys.*, *33*(4), 441–462, doi:10.1029/95RG02074.

Morse, P. H., and K. Ingard (1968), *Theoretical Acoustics*, 1st ed., McGraw-Hill, New York.

Olsen, K. B., A. Akinci, A. Rovelli, F. Marra, and L. Malagnini (2006), 3D ground-motion estimation in Rome, Italy, *Bull. Seismol. Soc. Am.*, *96*, 133–146, doi:10.1785/0120030243.

Owens, T. J., H. P. Crotwell, C. Groves, and P. Oliver-Paul (2004), SOD: Standing Order for Data, *Seismol. Res. Lett.*, *75*, 515–520, doi:10.1785/gssrl.75.4.515-a.

Paige, C. C., and M. A. Saunders (1982), LSQR: An algorithm for sparse linear equations and sparse least squares, *ACM Trans. Math. Softw.*, *8*, 43–71, doi:10.1145/355984.355989.

Phillips, W. S., and R. J. Stead (2008), Attenuation of Lg in the western US using the USArray, *Geophys. Res. Lett.*, *35*, L07307, doi:10.1029/2007GL032926.

Power, M., B. Chiou, N. A. Abrahamson, C. Roblee, Y. Bozorgnia, and T. Shantz (2008), An introduction to NGA, *Earthq. Spectra*, *24*, 3–21, doi:10.1193/1.2894833.

Pratt, T. L., and T. M. Brocher (2006), Site response and attenuation in the Puget Lowland, Washington State, *Bull. Seismol. Soc. Am.*, *96*(2), 536–552, doi:10.1785/0120040200.

Priestley, K., and D. McKenzie (2006), The thermal structure of the lithosphere from shear wave velocities, *Earth Planet. Sci. Lett.*, *244*, 285–301, doi:10.1016/j.epsl.2006.01.008.

Prieto, G. A., and G. C. Beroza (2008), Earthquake ground motion prediction using the ambient seismic field, *Geophys. Res. Lett.*, *35*, L14304, doi:10.1029/2008GL034428.

Prieto, G. A., J. F. Lawrence, and G. C. Beroza (2009), Anelastic Earth structure from the coherency of the ambient seismic field, *J. Geophys. Res.*, *114*, B07303, doi:10.1029/2008JB006067.

Pujol, J., and S. Smithson (1991), Seismic wave attenuation in volcanic rocks from VSP experiments, *Geophysics*, *56*, 1441–1455, doi:10.1190/1.1443164.

Rodriguez, B. D., and J. M. Williams (2001), *Deep regional resistivity structure across the Battle Mountain-Eureka and Carlin Trends, North-Central Nevada*, *U.S. Geol. Surv. Open File Rep., 01-0346*.

Romanowicz, B. Y. C. G. (2002), Superplumes from the core-mantle boundary to the lithosphere: Implications for heat flux, *Science*, *296*, 513–516, doi:10.1126/science.1069404.

Sabra, K. G., P. Roux, and W. A. Kuperman (2005a), Emergence rate of the time-domain Green's function from the ambient noise cross-correlation function, *J. Acoust. Soc. Am.*, *96*(3), 1182–1191.

Sabra, K. G., P. Gerstoft, P. Roux, W. A. Kuperman, and M. C. Fehler (2005b), Surface wave tomography from microseisms in Southern California, *Geophys. Res. Lett.*, *32*, L14311, doi:10.1029/2005GL023155.

Sanchez-Sesma, F. J., and M. Campillo (2006), Retrieval of the Green's function from cross correlation; the canonical elastic problems, *Bull. Seismol. Soc. Am.*, *96*(3), 1182–1191, doi:10.1785/0120050181.

Savage, J. C., and R. O. Burford (1973), Geodetic determination of relative plate motion in central California, *J. Geophys. Res.*, *78*, 832–845, doi:10.1029/JB078i005p00832.

Shapiro, N. M., M. Campillo, L. Stehly, and M. H. Ritzwoller (2005), High-resolution surface-wave tomography from ambient seismic noise, *Science*, *307*, 1615–1618, doi:10.1126/science.1108339.

Smith, R. B., and L. W. Braile (1994), The Yellowstone hotspot, *J. Volcanol. Geotherm. Res.*, *61*, 121–187, doi:10.1016/0377-0273(94)90002-7.

Snieder, R., and E. Safak (2006), Extracting the building response using seismic interferometry: Theory and application to the Millikan Library in Pasadena, California, *Bull. Seismol. Soc. Am.*, *96*(2), 586–598, doi:10.1785/0120050109.

Tian, Y., K. Sigloch, and G. Nolet (2009), Multiple-frequency SH-wave tomography of the western US upper mantle, *Geophys. J. Int.*, *178*, 1384–1402, doi:10.1111/j.1365-246X.2009.04225.x.

Tsai, V. C., and M. P. Moschetti (2010), An explicit relationship between time-domain noise correlation and spatial autocorrelation (SPAC) results, *Geophys. J. Int.*, *182*, 454–460.

Weaver, R. L., and O. I. Lobkis (2001), Ultrasonics without a source: Thermal fluctuation correlations at MHz frequencies, *Phys. Rev. Lett.*, *87*, 134301.

Weaver, R. L., and O. I. Lobkis (2004), Diffuse fields in open systems and the emergence of the greens function, *J. Acoust. Soc. Am.*, *116*(5), 2731–2734, doi:10.1121/1.1810232.

Xie, J. (2002), Lg Q in the eastern Tibetan Plateau, *Bull. Seismol. Soc. Am.*, *92*(2), 871–876, doi:10.1785/0120010154.

Yang, Y., and D. W. Forsyth (2008), Attenuation in the upper mantle beneath Southern California: Physical state of the lithosphere and asthenosphere, *J. Geophys. Res.*, *113*, B03308, doi:10.1029/2007JB005118.

Yang, Y., D. W. Forsyth, and D. S. Weeraratne (2007), Seismic attenuation near the East Pacific Rise and the origin of the low-velocity zone, *Earth Planet. Sci. Lett.*, *258*(1–2), 260–268, doi:10.1016/j.epsl.2007.03.040.

Yao, H., R. D. van der Hilst, and M. Van de Hoop (2006), Surface-wave array tomography in SE Tibet from ambient seismic noise and two-station analysis I. Phase velocity maps, *Geophys. J. Int.*, *166*, 732–744, doi:10.1111/j.1365-246X.2006.03028.x.

Yokoi, T., and S. Margaryan (2008), Consistency of spatial autocorrelation method with the seismic interferometry and its consequence, *Geophys. Prospect.*, *56*, 435–451, doi:10.1111/j.1365-2478.2008.00709.x.

Zheng, S., X. Sun, X. Song, Y. Yang, and M. H. Ritzwoller (2008), Surface wave tomography of China from ambient seismic noise correlation, *Geochem. Geophys. Geosyst.*, *9*, Q05020, doi:10.1029/2008GC001981.

J. F. Lawrence, Department of Geophysics, Stanford University, 397 Panama Mall, Stanford, CA 94305-2215, USA. (jflawrence@stanford.edu)

G. A. Prieto, Departamento de Física, Universidad de los Andes, Bogotá, Colombia.